Wang *et al. Microstructures* 2024;4:2024040
DOI: 10.20517/microstructures.2023.98

Microstructures

Research Article

Open Access

Check for updates

Control of exposed crystal planes of CeO_2 enhances electrocatalytic nitrate reduction

Fei Wang[1,2,#], **Dan Li**[1,#], **Jian Mao**[1]

[1]College of Materials Science and Engineering, Sichuan University, Chengdu 610065, Sichuan, China.
[2]Faculty of Materials Science and Engineering, Kunming University of Science and Technology, Kunming 650093, Yunnan, China.
[#]Authors contributed equally.

Correspondence to: Prof. Jian Mao, College of Materials Science and Engineering, Sichuan University, No. 24 South Section 1, Yihuan Road, Chengdu 610065, Sichuan, China. E-mail: maojian@scu.edu.cn; Prof. Fei Wang, Faculty of Materials Science and Engineering, Kunming University of Science and Technology, No. 727 Jingming South Road, Chenggong District, Kunming 650093, Yunnan, China. E-mail: echo1994wf@foxmail.com

How to cite this article: Wang F, Li D, Mao J. Control of exposed crystal planes of CeO_2 enhances electrocatalytic nitrate reduction. *Microstructures* 2024;4:2024040. https://dx.doi.org/10.20517/microstructures.2023.98

Received: 25 Dec 2023 **First Decision:** 27 Feb 2024 **Revised:** 12 Mar 2024 **Accepted:** 29 Mar 2024 **Published:** 4 Jul 2024

Academic Editor: Yida Deng **Copy Editor:** Fangyuan Liu **Production Editor:** Fangyuan Liu

Abstract

Cerium dioxide (CeO_2) has emerged as a promising electrocatalyst for electrocatalytic nitrate reduction to produce ammonia (NRA). However, the NRA performance of CeO_2 still needs to be improved and the interface-related NRA electrocatalytic activity of CeO_2 is unclear. Herein, CeO_2 with exposed (111) or (200)/(220) planes is prepared by adjusting the amount of added surfactant simply. The CeO_2 with exposed (220)/(200) planes presents higher NRA performance than that of CeO_2 with the exposed (111) plane. Based on density functional theory, the enhanced mechanism is revealed. The exposed (111) plane of CeO_2 repels NO_3^-, interrupting the following NRA processes. For exposed (200)/(220) planes of CeO_2, they show high affinity for NO_3^- and relatively low energy barriers for NRA reactions, bringing about enhanced NRA performance. This work shows a crystal-plane-dependent strategy for enhancing the catalytic performance of electrocatalysts.

Keywords: Exposed crystal plane, electrocatalytic nitrate reduction, CeO_2, DFT

INTRODUCTION

Nitrate pollution poses a major threat to water resources and ecosystems, leading to adverse health effects and ecological imbalances[1,2]. By utilizing electrocatalytic reduction, nitrate can be converted into ammonia

(NH_3) efficiently, which is widely used as a fertilizer and precursor for various industrial processes[3,4]. This approach offers a promising alternative to traditional methods of NH_3 production, such as the energy-intensive Haber-Bosch process which consumes large amounts of fossil fuels and emits greenhouse gases[5-7]. The electrocatalytic and thermal catalytic nitrate reduction to produce NH_3 (NRA) provides a greener and sustainable pathway for NH_3 production but also presents from nitrate pollution[8-10]. In contrast, thermal catalytic NRA requires a hydrogen source, leading to high complexity of the catalytic device. The electrocatalytic NRA operates with a simple experimental device driven by green electric energy, and it looks more promising. Nevertheless, due to the involvement of an eight-electron transfer, the electrocatalytic reaction exhibits complex reaction pathways and intermediates, and the competitive hydrogen evolution reaction (HER) weakens the electrocatalytic efficiency[11-13]. As a result, there is an urgent need to design electrocatalysts with high efficiency and selectivity for NH_3 synthesis.

Cerium dioxide (CeO_2), as a rare earth metal oxide, possesses a distinctive crystal structure, such as the flexible conversion between Ce^{4+} and Ce^{3+}[14-16]. These unique characteristics contribute to its excellent redox properties and high oxygen mobility and make it highly valuable in various electrochemical fields[17-22]. Electrocatalytic procedures are interface reactions conducted on the exposed planes of electrocatalysts. Many works have found that catalytic performance is strongly dependent on the exposed crystal planes, because the exposed planes would interact with the reactants/intermediates resulting in different adsorption energy, Gibbs free energy and activity of competitive/side reactions[23,24]. Therefore, the NRA performance can be enhanced by controlling the exposed crystal planes. Moreover, the effect mechanism of different exposed crystal planes of CeO_2 on the NRA processes remains ambiguous.

Herein, the exposed crystal planes of CeO_2 are controlled by adjusting the quantity of cetyltrimethylammonium bromide (CTAB), and CeO_2 with exposed (111) plane or (220)/(200) planes is prepared. The CeO_2 with exposed (220)/(200) planes presents higher NRA performance than that of CeO_2 with the (111) plane. Compared with the CeO_2 with exposed (111) plane, the NH_3 yield rate ($Yield_{NH3}$) and Faraday efficiency (FE) of CeO_2 with exposed (200)/(220) planes increase by 11.9% and 37.7%, respectively. Density functional theory (DFT) is used to reveal the underlying mechanism. This work paves a new pathway for designing high-performance NRA electrocatalysts.

EXPERIMENTAL DETAILS

Preparation of CeO_2

First, 0.87 g of $Ce(NO_3)_3 \cdot 6H_2O$ was dissolved in 60 mL of ethanol to obtain solution A. In a separate container, a specific amount of CTAB (0.5, 1.0, or 2.0 g), formic acid (575 uL), and dimethylamine (495 uL) were mixed in ethanol (60 mL) to obtain solution B. Solution A was then added into solution B with stirring (30 min) to obtain a mixture. Subsequently, the mixture was stood overnight to obtain the precipitate. The precipitate was washed and dried (80 °C), and the materials were sintered at 500 °C in an air atmosphere for 3 h. The resulting products were marked as CeO_2-CTAB0.5, CeO_2-CTAB1.0, and CeO_2-CTAB2.0, corresponding to the different amounts of CTAB used in the synthesis process.

Characterization

X-ray diffraction (XRD) patterns were obtained using a D8 Advance diffractometer (Bruker, Germany) equipped with Cu Kα radiation. Scanning electron microscopy (SEM) images were acquired with a ZEISS MERLIN Compact microscope (Zeiss, Germany). The Brunauer-Emmett-Teller (BET) tests were performed with an ASAP2460 instrument (Micromeritics, USA). Transmission electron microscopy (TEM) images were captured using a FEI Tecnai G2 F20 microscope (FEI, USA). The thermogravimetric analysis (TGA) and differential scanning calorimetry (DSC) curves were obtained through testing on the TGA5500

instrument (TA, USA). NH_4^+ concentrations were measured employing a UV-1700 spectrophotometer (SHIMAZHU, Japan). Electron paramagnetic resonance spectroscopy (EPR) testing was used to test the oxygen vacancies of the samples and was performed on a Bruker A300 (Bruker, Germany). Other details for characterizations and calculations were described in the Supporting Material.

Electrochemical tests

Electrochemical tests were conducted using an Interface 1010E electrochemical workstation (Gamry, USA) with an H-type electrolytic cell. The three-electrode system comprised a sample as the working electrode, a platinum sheet as the counter electrode, and the Hg/HgO as the reference electrode. All measured potentials were converted to the reversible hydrogen electrode (RHE) scale, determined by E(RHE) = E(Hg/HgO) + 0.059 × pH + 0.098. To prepare the working electrode, a dispersion was created by combining 5 mg of the samples with 50 μL Nafion solution (5 wt%) in 450 μL of ethanol. Then, 100 μL droplets of the dispersion were carefully transferred onto 1 × 1 cm^2 carbon paper. The loading mass of the working electrode was around 0.2 mg. For electrochemical testing, 50 mL electrolyte (0.1 M Na_2SO_4) was added to the anodic electrolytic cell, and 50 mL electrolyte (0.1 M Na_2SO_4 and $NaNO_3$) was added to the cathodic electrolytic cell. The electrolyte type, pH and concentration setting is the same as the related work[25]. Before testing, argon gas was bubbled through the electrolyte to remove any traces of nitrogen. Linear sweep voltammetry (LSV) was performed with a scan rate of 10 mV/s, and potentiostatic testing was conducted at a constant potential for an hour. Subsequently, the electrolyte after the tests was subjected to UV-Vis light analysis to calculate the $Yield_{NH_3}$ and FE. The stirring rate remained constant for all tests.

RESULTS AND DISCUSSION

Figure 1A-C presents the SEM images of the samples; it is evident that the samples predominantly consist of nearly spherical agglomerates. These agglomerates exhibit a wide size distribution, ranging from around 100 to 400 nm. Additionally, with increasing amounts of CTAB, no significant change in the morphology and size of agglomerates indicates that the amount of CTAB has little effect on its morphology and size. The XRD patterns show that the precursor material is cerium formate, which transforms into CeO_2 upon calcination [Figure 1D]. The peaks at 28.6°, 33.2°, 47.6°, 56.5°, 59.2°, 69.4°, 76.9°, 79.3° and 88.6° correspond to (111), (200), (220) (311), (222), (400), (331), (420) and (422) planes of CeO_2 (PDF 34#0394), respectively. Figure 1E and F demonstrates the N_2 adsorption/desorption isotherm curves and pore size distribution curves of samples. Based on the classification of International Union of Pure and Applied Chemistry (IUPAC) adsorption isotherms, those curves correspond to the type III adsorption model indicating the porous nature of samples[26]. BET specific surface areas of CeO_2-CTAB0.5, CeO_2-CTAB1.0, and CeO_2-CTAB2.0 are 83, 97, and 87 m^2/g, respectively, and the average pore diameters calculated by the Barrett-Joyner-Halenda (BJH) method are 16.3, 16.0 and 13.8 nm, respectively. Therefore, adding CTAB does not significantly influence the morphology, size and specific surface area of CeO_2, and its effect on the NRA performance of CeO_2 can be disregarded.

To further investigate the microstructure of CeO_2 and assess its influence on performance, TEM testing was conducted [Figure 2]. Figure 2A-C further reveals the aggregation of smaller structures. Interestingly, the ratio of rod-shaped CeO_2 increases significantly with the rising amount of CTAB. For the small granular CeO_2, the observed interplanar spacing is 0.312 nm [Figure 2D], which corresponds to its (111) crystal plane. This crystal plane is considered the most stable low-index plane for CeO_2 and is exposed typically on granular CeO_2 surfaces[27,28]. For the rod-shaped CeO_2, the observed interplanar spacing is primarily 0.269 nm corresponding to the (200) crystal plane [Figure 2E and F]. Additionally, for clearly identifiable single-crystal particles, fast Fourier transform (FFT) analysis can be applied to analyze the top and bottom exposed planes[29]. The norms of the vectors depicted in Figure 2E are all 0.269 nm, corresponding to the

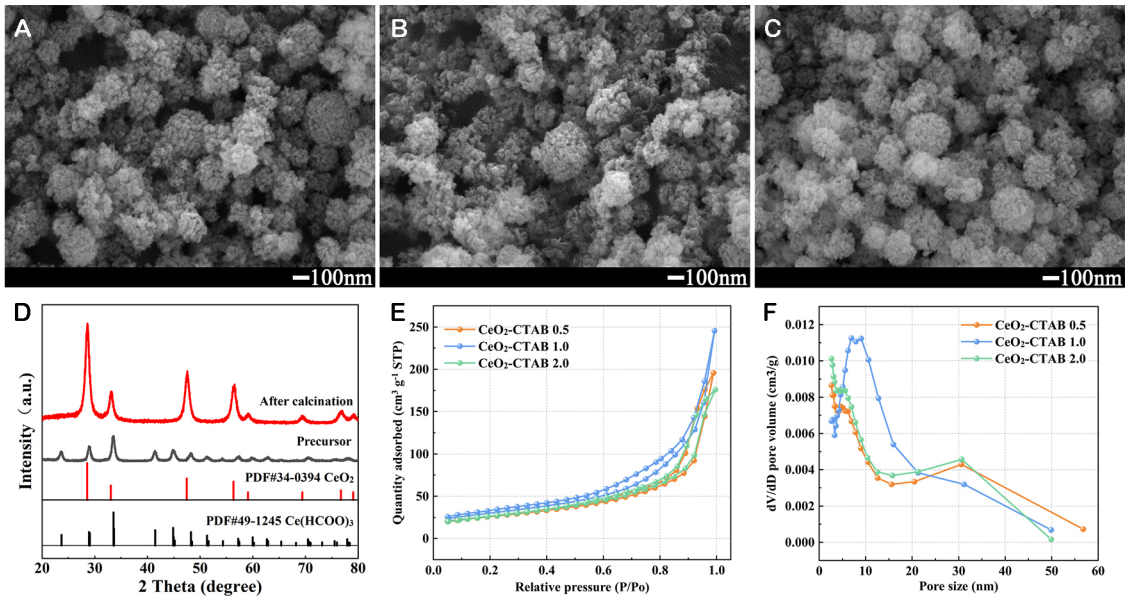

Figure 1. SEM image of (A) CeO_2-CTAB0.5, (B) CeO_2-CTAB1.0 and (C) CeO_2-CTAB2.0. (D) XRD patterns of precursor and calcined product of CeO_2-CTAB 1.0. (E) The N_2 adsorption and desorption isotherm curves. (F) Pore size distribution curves of CeO_2.

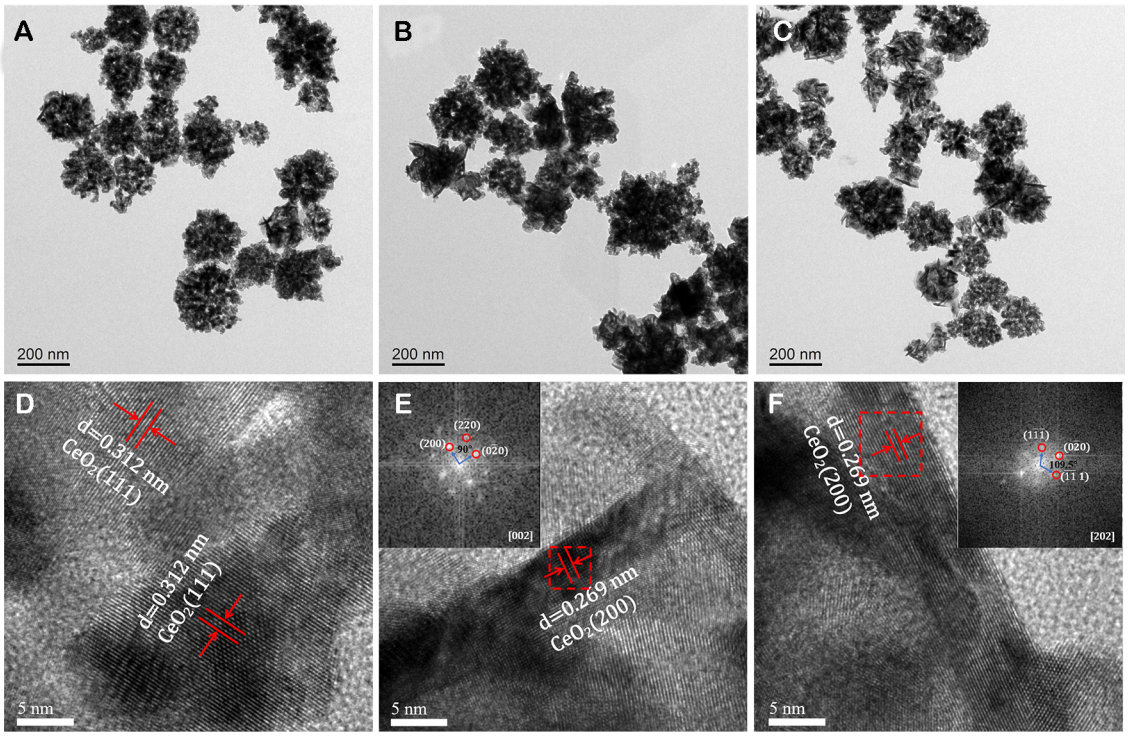

Figure 2. TEM morphology of (A) CeO_2-CTAB0.5, (B) CeO_2-CTAB1.0 and (C) CeO_2-CTAB2.0. HR-TEM of (D) granular CeO_2 and (E and F) rod-shaped CeO_2 in CeO_2-CTAB1.0.

interplanar spacing of the (200) and (0$\bar{2}$0) crystal planes. The angle between the vectors representing the (200) and (0$\bar{2}$0) planes is measured as 90°, matching the interfacial angle between the (200) and (0$\bar{2}$0) crystal faces. Therefore, the zone axis perpendicular to the diffraction plane can be identified as the [002] axis,

which confirms that the exposed top and bottom surfaces of the rod-shaped CeO_2 [Figure 2E] correspond to the (002) crystal plane. Likewise, it can be deduced that the top and bottom exposed surfaces of the rod-shaped CeO_2 shown in Figure 2F are (202) surfaces. Thus, the primary exposed surfaces of the rod-shaped CeO_2 are mainly (200) and (220), while that for granular CeO_2 is (111). The results align with previous studies[30,31].

To determine whether the rod-shaped CeO_2 structures are formed during the precipitation or calcination process, TEM testing was also conducted on the cerium formate precursor [Figure 3A]. However, no rod-shaped morphology is observed in the precursor, suggesting that the formation of rod-shaped CeO_2 structures occurs during subsequent calcination rather than inherited by the precipitation, and the presence of a mushy substance on the surface indicates the presence of CTAB. The DSC/TGA curves of the precursor [Figure 3B] reveal that the main decomposition temperature of $Ce(HCOO)_3$ is approximately 320 °C, and previous weight loss is primarily due to dehydration and CTAB decomposition[32]. Based on these findings, the calcination process was adjusted (two-hour calcination at 300 °C followed by one-hour calcination at 500 °C). As a result, all the rod-shaped CeO_2 structures disappear [Figure 3C], and the exposed crystal faces of small particles are (111) plane [Figure 3D]. This outcome can be attributed to the complete decomposition of CTAB at 300 °C, which effectively halts its contribution to the subsequent growth of CeO_2. When the CTAB is removed ahead, the growth of CeO_2 would be along the (111) crystal plane with the lowest energy[33]. With the adsorption of CTAB, the growth of the (111) crystal plane is obstructed, and its growth would follow other directions to form the rod shape.

The NRA performance of prepared catalysts is evaluated. LSV results [Figure 4A] reveal a significant increase in current density at the same potential after the addition of NO_3^- to the electrolyte, indicating the pronounced NRA performance of CeO_2. In the absence of NO_3^-, CeO_2-CTAB2.0 exhibits a significant decrease in current density at the same potential, indicating minimal competition from HER[34]. The LSV curves of the catalysts in the Na_2SO_4 electrolyte are shown in Supplementary Figure 1A. When the current density reaches 10 mA, the overpotential of the three catalysts is -1.14, -1.03 and -1.21 V, respectively, and the corresponding Tafel slopes are 471, 536 and 527 mV dec^{-1}, respectively Supplementary Figure 1B, further confirming their very poor catalytic HER activity. The HER starting potential occurs at approximately -1.0 V (corresponding to a current density of 10 mA cm^{-2}). Hence, The -1.0 V is selected as the starting potential to ensure high FE and $Yield_{NH_3}$. Based on the UV-Vis curves of solutions with various NH_4^+ concentrations [Supplementary Figure 2], the obtained calibration curve with a high R^2 value (0.99905) is presented in Figure 4B. After potentiostatic tests [Supplementary Figures 3-5], the corresponding $Yield_{NH_3}$ and FE are calculated [Figure 4C-E]. With increasing amounts of CTAB during preparation, both the $Yield_{NH_3}$ and FE of the obtained CeO_2 show improvement. The maximum $Yield_{NH_3}$ and FE are 460 μmol h^{-1} mg^{-1} and 39.1%, respectively. These enhancements can be attributed to the presence of more rod-shaped CeO_2 structures [(220)/(200) exposed planes] in the CeO_2-CTAB2.0 (discussed later). Furthermore, the cycling performance of CeO_2-CTAB2.0 is assessed [Figure 4F]. After five cycles, there is no significant decrease in both $Yield_{NH_3}$ and FE, indicating its excellent stability. The chronoamperometry curves and $Yield_{NH_3}$ of various catalysts in electrolytes with and without NO_3^- are shown in Supplementary Figure 6. It can be seen that when the electrolyte does not contain nitrate, the current is very weak, and the $Yield_{NH_3}$ is less than 50 umol h^{-1} cm^{-2}. Considering errors in experiments, the $Yield_{NH_3}$ can be almost negligible. Therefore, it can be inferred that the produced NH_3 is mainly from NO_3^- of the electrolyte. Based on the CV curves at various scanning rates, the electrochemical active area (ECSA) of CeO_2-CTAB0.5, CeO_2-CTAB1.0 and CeO_2-CTAB2.0 are estimated [Supplementary Figure 7], and the values are 1.75, 3.25 and 2.25 cm^2. The CeO_2-CTAB1.0 presents the highest ECSA, while its NRA performance is not the highest,

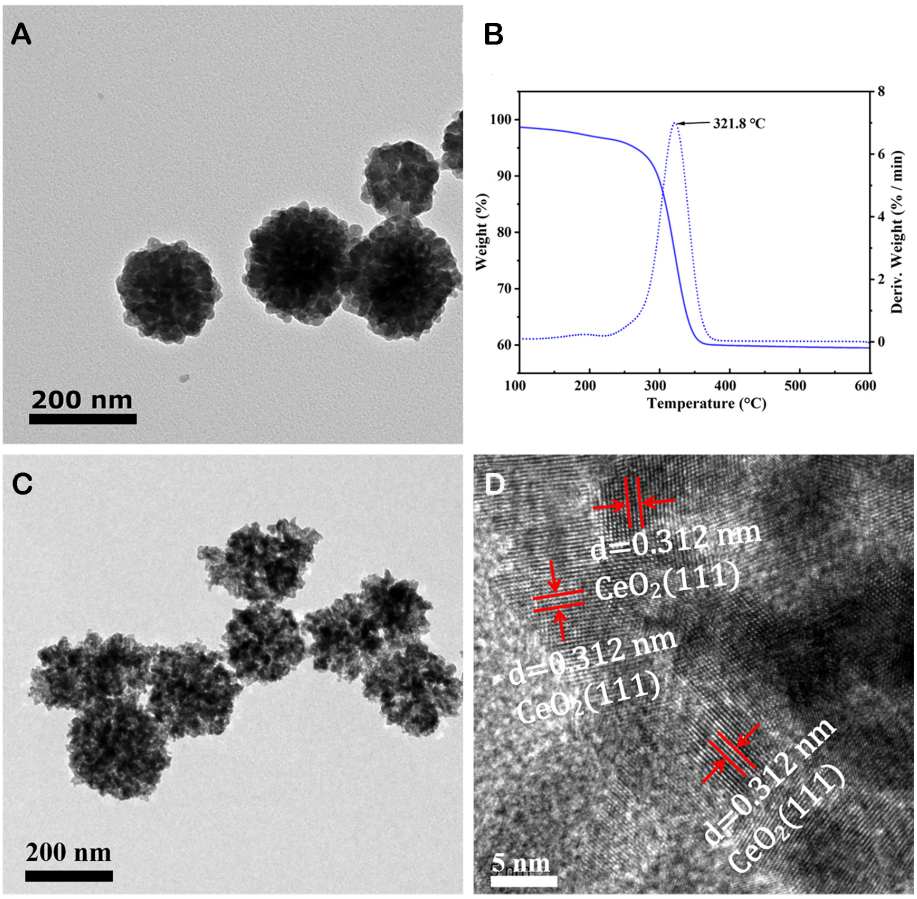

Figure 3. (A) TEM morphology and (B) TGA/DSC curves of cerium formate precursor. (C) TEM and (D) HRTEM morphology of CeO_2-CTAB2.0 (2-h calcination at 300 °C followed by 1-h calcination at 500 °C).

indicating that the NRA performance of CeO_2 is majorly determined by exposed crystal planes. The long-term stability test (-1.05 V) of CeO_2-CTAB2.0 is shown in Supplementary Figure 8, and the current density only slightly increases. In the split XPS Ce 3d spectra [Supplementary Figure 9A], u0, u2, u3, v0, v2 and v3 peaks are the spin-orbit splitting peaks of Ce^{4+}, and u1 and v1 peaks are the signal of Ce^{3+}. Before and after testing, the XPS Ce 3d spectra are almost overlapped. In the XPS O 1s spectra [Supplementary Figure 9B], the peaks at 529.4, 530.8, and 532.4 eV represent lattice oxygen, vacancy oxygen, and adsorbed oxygen, respectively. The intensity ratio of vacancy oxygen and lattice oxygen is almost constant before and after testing. The EPR results [Supplementary Figure 9C] also show that the oxygen vacancy concentration remained basically unchanged before and after the performance test[35]. The above results confirm its catalytic stability.

DFT calculations are employed to investigate the effect of exposed crystal planes on NRA. The calculated model of CeO_2 is shown in Supplementary Figure 10. Based on TEM analysis results, 2 × 2 surfaces of CeO_2 (111), (200), and (220) planes are considered for the calculation processes [Supplementary Figure 11]. The adsorption energies of H and NO_3^- on different exposed surfaces of CeO_2 are initially examined [Figure 5A]. The adsorption for NO_3^- and H is the first step for the conventional and surface hydrogenation mechanisms, respectively, and the high adsorption energy (E_{ad}) for NO_3^- is necessary for the NRA. The CeO_2 (111) plane

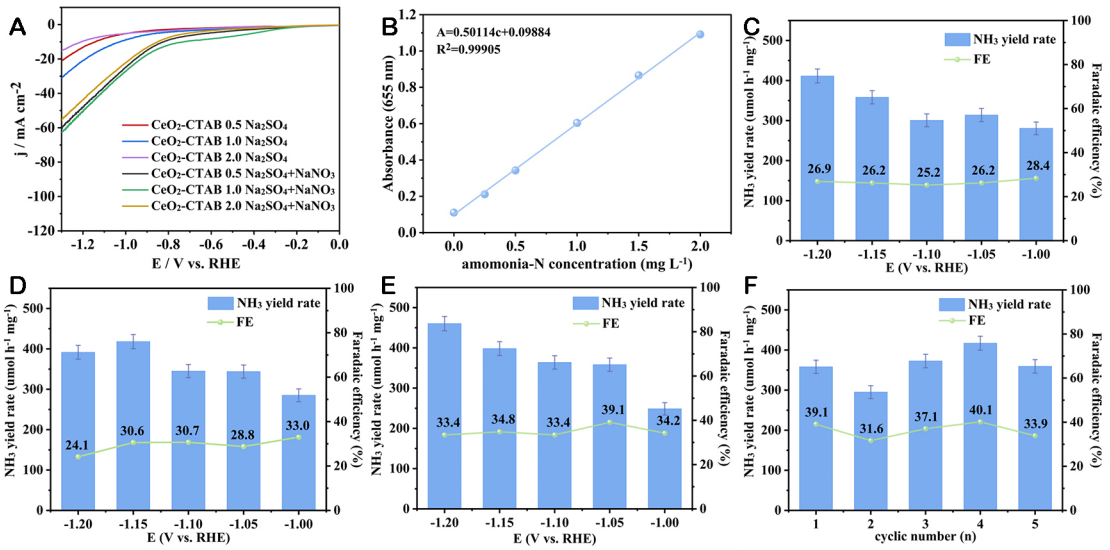

Figure 4. (A) LSV curves of CeO_2 in a 0.5 M Na_2SO_4 electrolyte with and without NO_3^-. (B) Calibration curve used for estimation of ammonia-N concentration. (C-E) are potential-dependent FE_{NH3} and $Yield_{NH3}$ over CeO_2-CTAB0.5, CeO_2-CTAB1.0 and CeO_2-CTAB2.0. (F) The cyclic stability test of CeO_2-CTAB2.0 at -1.05 V.

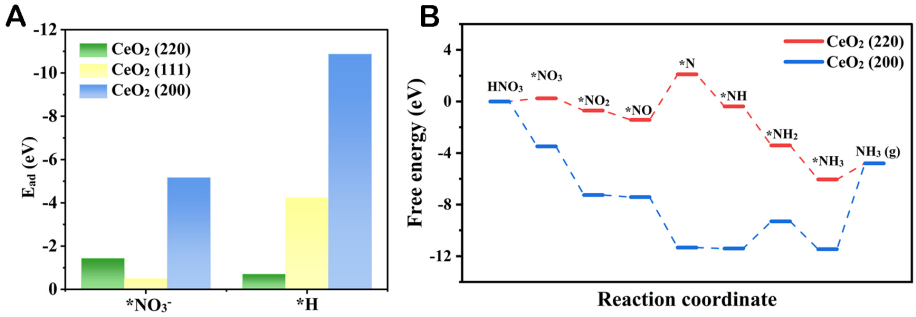

Figure 5. (A) Adsorption energy of NO_3^- and H on CeO_2 (200), (220) and (111) planes. (B) Gibbs free energy diagrams of different intermediates generated during NRA on CeO_2 (200) and CeO_2 (220) planes.

presents weak adsorption for NO_3^-, and it is hard to conduct NRA reactions. The E_{ad} for H and NO_3^- is comparable to the CeO_2 (200) plane. For the (220) plane, the adsorption for NO_3^- is strong while the adsorption for H is weak. The results indicate that the NRA on the CeO_2 (220) and (200) planes may be conducted by gradually continuous and surface hydrogenation mechanisms, respectively[36].

The change of Gibbs free energy throughout the entire NRA reactions is calculated for (200) and (220) planes [Figure 5B] and the configurations are shown in Supplementary Figures 12 and 13. For the CeO_2 with (220) plane, the rate-determining step (RDS) is *NO to *N step with an energy barrier of 3.5 eV. For the CeO_2 with (200) plane, the RDS is *NH to *NH_2 step with an energy barrier of 2.1 eV. For the aspect of free energy, the NRA tends to occur on the CeO_2 (200) plane. The energy barrier (2.1 eV) is close to many reported high-performance NRA electrocatalysts, such as TiO_2[37], Rh[38], and $NiCo_2O_4$[39]. The improved NRA performance observed in experiments is attributed to the high affinity for NO_3^- and relatively low energy barrier.

CONCLUSIONS

In this work, the exposed crystal planes of CeO_2 are controlled by adjusting the amount of added CTAB. With the increase of CTAB, the exposed crystal planes of CeO_2 are transferred from (111) to (200)/(220) planes. This transition occurred due to the obstruction of the growth of the (111) crystal plane by the adsorbed CTAB.

The CeO_2 with exposed (220)/(200) planes presents higher NRA performance than that of CeO_2 with the (111) plane. Compared with the CeO_2 with exposed (111) plane, the $Yield_{NH3}$ and FE of CeO_2 with exposed (200)/(220) planes increase by 11.9% and 37.7%, respectively. DFT is used to reveal the underlying mechanism. The exposed (111) plane of CeO_2 is hard to adsorb NO_3^-, while both exposed (200)/(220) planes of CeO_2 show high affinity for NO_3^- and relatively low energy barriers along the NRA pathways, bringing about enhanced NRA performance. This work shows an effective way to improve the catalytic performance of electrocatalysts.

DECLARATIONS

Acknowledgments

The authors thank the Analytical & Testing Center of Sichuan University (CASTEP).

Authors' contributions

Conceived and designed the study: Mao J, Li D, Wang F
Prepared the samples and collected the data: Li D
Performed data analysis and wrote the main draft of the paper: Li D, Wang F
All authors discussed the results and commented on the manuscript.

Availability of data and materials

Not applicable.

Financial support and sponsorship

This work was supported by the "Natural Science Foundation of Sichuan Province" [24NSFSC3150], the "2021 Strategic Cooperation Project between Sichuan University and The People's Government of Luzhou" [2021CDLZ-1], and "Special Funding for Postdoctoral Research Project of Sichuan Province" [TB2023053].

Conflicts of interest

All authors declared that there are no conflicts of interest.

Ethical approval and consent to participate

Not applicable.

Consent for publication

Not applicable.

REFERENCES

1. Huang Y, Liu S, Pei M, Li J, Xu H, Chen Y. Unveiling H_2O_2-optimized NO_x adsorption-selective catalytic reduction (AdSCR) performance of $WO_3/CeZrO_2$ catalyst. *Rare Met* 2023;42:3755-65. DOI
2. Ju L, Tang X, Kou L. Polarization boosted catalysis: progress and outlook. *Microstructures* 2022;2:2022008. DOI

3. Li X, Shen P, Li X, Ma D, Chu K. Sub-nm RuO_x clusters on Pd metallene for synergistically enhanced nitrate electroreduction to ammonia. *ACS Nano* 2023;17:1081-90. DOI
4. Wu Y, Yao K, Zhao Z, et al. Efficient electrocatalytic reduction of nitrate to ammonia over Mo_2CT_x micro-foam with rich edge sites. *Chem Eng J* 2024;479:147602. DOI
5. Soloveichik G. Electrochemical synthesis of ammonia as a potential alternative to the Haber-Bosch process. *Nat Catal* 2019;2:377-80. DOI
6. Luo H, Li S, Wu Z, et al. Modulating the active hydrogen adsorption on Fe-N interface for boosted electrocatalytic nitrate reduction with ultra-long stability. *Adv Mater* 2023;35:e2304695. DOI
7. Wu Z, Song Y, Guo H, et al. Tandem catalysis in electrocatalytic nitrate reduction: unlocking efficiency and mechanism. *Interdiscip Mater* 2024;3:245-69. DOI
8. Sun L, Liu B. Mesoporous PdN alloy nanocubes for efficient electrochemical nitrate reduction to ammonia. *Adv Mater* 2023;35:e2207305. DOI PubMed
9. Yang G, Zhou P, Liang J, Li H, Wang F. Opportunities and challenges in aqueous nitrate and nitrite reduction beyond electrocatalysis. *Inorg Chem Front* 2023;10:4610-31. DOI
10. Liang X, Zhu H, Yang X, et al. Recent advances in designing efficient electrocatalysts for electrochemical nitrate reduction to ammonia. *Small Struct* 2023;4:2200202. DOI
11. Zhou J, Wen M, Huang R, et al. Regulating active hydrogen adsorbed on grain boundary defects of nano-nickel for boosting ammonia electrosynthesis from nitrate. *Energy Environ Sci* 2023;16:2611-20. DOI
12. Peng O, Hu Q, Zhou X, et al. Swinging hydrogen evolution to nitrate reduction activity in molybdenum carbide by ruthenium doping. *ACS Catal* 2022;12:15045-55. DOI
13. Yang R, Li H, Long J, Jing H, Fu X, Xiao J. Potential dependence of ammonia selectivity of electrochemical nitrate reduction on copper oxide. *ACS Sustain Chem Eng* 2022;10:14343-50. DOI
14. Masuda T, Fukumitsu H, Fugane K, et al. Role of cerium oxide in the enhancement of activity for the oxygen reduction reaction at Pt-CeO_x nanocomposite electrocatalyst-An in situ electrochemical X-ray absorption fine structure study. *J Phys Chem C* 2012;116:10098-102. DOI
15. Zhu Y, Liu S, Jin C, Bie S, Yang R, Wu J. MnO_x decorated CeO_2 nanorods as cathode catalyst for rechargeable lithium-air batteries. *J Mater Chem A* 2015;3:13563-7. DOI
16. Lu G, Zheng H, Lv J, Wang G, Huang X. Review of recent research work on CeO_2-based electrocatalysts in liquid-phase electrolytes. *J Power Sources* 2020;480:229091. DOI
17. Zhou A, Wang D, Li Y. Hollow microstructural regulation of single-atom catalysts for optimized electrocatalytic performance. *Microstructures* 2021;2:2022005. DOI
18. Bi H, Yin X, He J, et al. Conjugated organic component-functionalized hourglass-type phosphomolybdates for visible-light photocatalytic Cr(VI) reduction in wide pH range. *Rare Met* 2023;42:3638-50. DOI
19. Xie H, Wang H, Geng Q, et al. Oxygen vacancies of Cr-Doped CeO_2 nanorods that efficiently enhance the performance of electrocatalytic N_2 fixation to NH_3 under ambient conditions. *Inorg Chem* 2019;58:5423-7. DOI
20. Liu Y, Li C, Guan L, Li K, Lin Y. Oxygen vacancy regulation strategy promotes electrocatalytic nitrogen fixation by doping Bi into Ce-MOF-Derived CeO_2 nanorods. *J Phys Chem C* 2020;124:18003-9. DOI
21. Wang X, Sun C, He F, et al. Enhanced hydrogen evolution reaction performance of $NiCo_2P$ by filling oxygen vacancies by phosphorus in thin-coating CeO_2. *ACS Appl Mater Interfaces* 2019;11:32460-8. DOI
22. Shi Y, Fu J, Hui K, et al. Promoting the electrochemical properties of yolk-shell-structured CeO_2 composites for lithium-ion batteries. *Microstructures* 2021;1:2021005. DOI
23. Zhang W, Shen Y, Pang F, et al. Facet-dependent catalytic performance of Au nanocrystals for electrochemical nitrogen reduction. *ACS Appl Mater Interfaces* 2020;12:41613-9. DOI
24. Wu T, Stone ML, Shearer MJ, et al. Crystallographic facet dependence of the hydrogen evolution reaction on CoPS: theory and experiments. *ACS Catal* 2018;8:1143-52. DOI
25. Gong Z, Zhong W, He Z, et al. Regulating surface oxygen species on copper (I) oxides via plasma treatment for effective reduction of nitrate to ammonia. *Appl Catal B Environ* 2022;305:121021. DOI
26. Rahman MM, Muttakin M, Pal A, Shafiullah AZ, Saha BB. A statistical approach to determine optimal models for IUPAC-classified adsorption isotherms. *Energies* 2019;12:4565. DOI
27. Sayle DC, Maicaneanu SA, Watson GW. Atomistic models for CeO_2(111), (110), and (100) nanoparticles, supported on yttrium-stabilized zirconia. *J Am Chem Soc* 2002;124:11429-39. DOI
28. Lundberg M, Skårman B, Reine Wallenberg L. Crystallography and porosity effects of CO conversion on mesoporous CeO_2. *Microporous Mesoporous Mater* 2004;69:187-95. DOI
29. Qu J, Wang Y, Mu X, et al. Determination of crystallographic orientation and exposed facets of titanium oxide nanocrystals. *Adv Mater* 2022;34:e2203320. DOI
30. Mai HX, Sun LD, Zhang YW, et al. Shape-selective synthesis and oxygen storage behavior of ceria nanopolyhedra, nanorods, and nanocubes. *J Phys Chem B* 2005;109:24380-5. DOI
31. Zhou K, Wang X, Sun X, Peng Q, Li Y. Enhanced catalytic activity of ceria nanorods from well-defined reactive crystal planes. *J Catal* 2005;229:206-12. DOI

32. Sui Z, Chen X, Wang L, et al. Capping effect of CTAB on positively charged Ag nanoparticles. *Physica E Low Dimens Syst Nanostruct* 2006;33:308-14. DOI
33. Bakshi MS. How surfactants control crystal growth of nanomaterials. *Cryst Growth Des* 2016;16:1104-33. DOI
34. Li T, Li J, Zhang L, et al. Work-function-induced interfacial electron redistribution of MoO_2/WO_2 heterostructures for high-efficiency electrocatalytic hydrogen evolution reaction. *Rare Met* 2024;43:489-99. DOI
35. Guo Z, Yu Y, Li C, et al. Deciphering structure-activity relationship towards CO_2 electroreduction over SnO_2 by a standard research paradigm. *Angew Chem Int Ed* 2024;63:e202319913. DOI
36. Ling C, Zhang Y, Li Q, Bai X, Shi L, Wang J. New mechanism for N_2 reduction: the essential role of surface hydrogenation. *J Am Chem Soc* 2019;141:18264-70. DOI
37. García-mota M, Vojvodic A, Metiu H, et al. Tailoring the activity for oxygen evolution electrocatalysis on rutile TiO_2 (110) by transition-metal substitution. *ChemCatChem* 2011;3:1607-11. DOI
38. Li T, Han S, Cheng C, et al. Sulfate-enabled nitrate synthesis from nitrogen electrooxidation on a rhodium electrocatalyst. *Angew Chem Int Ed* 2022;134:e202204541. DOI
39. Liu Q, Xie L, Liang J, et al. Ambient ammonia synthesis via electrochemical reduction of nitrate enabled by $NiCo_2O_4$ nanowire array. *Small* 2022;18:e2106961. DOI